

# Preparation of Ultrathin and Degradable Polymeric Films by Electropolymerization of 3-Amino-L-tyrosine

Tommaso Marchesi D'Alvise, Sruthi Sunder, Roger Hasler, Julia Moser, Wolfgang Knoll, Christopher V. Synatschke, Sean Harvey,\* and Tanja Weil\*

Bioderived polymers are one of many current research areas that promise a sustainable future. Due to their unique properties, the bioderived polymer polydopamine has been in the spotlight over the last decades. Its ability to adhere to virtually any surface and its stability over a wide pH range as well as in several organic solvents make it a suitable candidate for various applications like coatings and biosensors. However, strong light absorption over a broad range of wavelengths and high quenching efficiency limit its uses. Therefore, new bioderived polymers with similar features to polydopamine but without fluorescence quenching properties are highly desirable. Herein, the electropolymerization of a bioderived analog of dopamine, 3-amino-L-tyrosine, is demonstrated. The resulting polymer, poly(amino-L-tyrosine), exhibits several characteristics complementary to or even exceeding those of polydopamine and its analog, polynorepinephrine, rendering poly(amino-L-tyrosine) attractive for the development of sensors and photoactive devices. Cyclic voltammetry, spectro-electrochemistry, and electrochemical quartz crystal microbalance measurements are applied to study the electrodeposition of this material, and the resulting films are compared to polydopamine and polynorepinephrine. Impedance spectroscopy reveals increased ion permeability of poly(amino-L-tyrosine) compared to polydopamine and polynorepinephrine. Moreover, the reduced fluorescence quenching of poly(amino-L-tyrosine) supports its use as coating for biosensors and organic semiconductors.

## 1. Introduction


The great demand of our society for more environmentally friendly and green processes has inspired new research in bioderived polymeric materials. Industrial extraction and processing techniques for high molecular weight and structurally complex biopolymers such as cellulose, chitin, and carbohydrates were developed in recent decades, but they often require large quantities of hazardous chemicals and produce extensive amounts of waste. In contrast, small bioderived molecules have attracted increasing attention as raw material for the bottom-up synthesis of polymers, because their material properties can be controlled with minimal waste production.<sup>[1,2]</sup> Although compounds such as terpenes and furans are derived from biostocks and have already shown great promise for the synthesis of commodity plastics including poly(ethylene terephthalate) (PET) and polyethylene (PE), there is a growing interest in new bioderived and biodegradable polymeric materials for specialty applications.<sup>[1–3]</sup> Phenol- and catechol-based compounds are ubiquitous in nature and can either be transformed into high-value chemicals or directly

polymerized into functional materials.<sup>[4–6]</sup> In particular, the amino acid L-tyrosine is an important molecule not only in the biosynthesis of many natural compounds, but also increasingly for the synthesis of bioderived materials.<sup>[7,8]</sup> For instance, dopamine, a neurotransmitter originating from L-tyrosine, has received much interest as a monomer for bioinspired polymer synthesis.<sup>[9,10]</sup> Dopamine is a major component of the mussel's byssus contributing to its unique ability to adhere to wet rocks.<sup>[11]</sup> Polydopamine (PDA) reveals similar adhesive properties and has been under intense investigation in recent years because it can be readily prepared by self-oxidative polymerization under alkaline conditions.<sup>[11]</sup> PDA adheres to almost every surface and shows good stability in aqueous solutions over a wide pH range of pH 2–10 as well as in many organic solvents. These properties have made PDA a suitable candidate for various applications, particularly as coatings for medical devices,<sup>[12]</sup> membranes, and biosensors, because it allows the tailoring of the surface properties of the target substrate.<sup>[13,14]</sup> In addition to

T. Marchesi D'Alvise, S. Sunder, J. Moser, C. V. Synatschke, S. Harvey, T. Weil

Department for Synthesis of Macromolecules  
 Max Planck Institute for Polymer Research  
 Ackermannweg 10, 55128 Mainz, Germany  
 E-mail: sdharv@gmail.com; tweil@mpip-mainz.mpg.de

R. Hasler, W. Knoll  
 Austrian Institute of Technology GmbH  
 Biosensor Technologies, Tulln 3430, Austria

 The ORCID identification number(s) for the author(s) of this article can be found under <https://doi.org/10.1002/marc.202200332>

© 2022 The Authors. Macromolecular Rapid Communications published by Wiley-VCH GmbH. This is an open access article under the terms of the Creative Commons Attribution License, which permits use, distribution and reproduction in any medium, provided the original work is properly cited.

DOI: 10.1002/marc.202200332

oxidative polymerization, PDA can also be produced by electrochemical methods, such as cyclic voltammetry (CV), in which a potential is swept between two vertices for several cycles.<sup>[15,16]</sup> In comparison to oxidative self-polymerization, the electrodeposition of dopamine proceeds faster, can be achieved in acidic solution, and affords more homogeneous films allowing also a more precise control of the thickness. Therefore, this method is very useful for coating different conductive substrates for various applications.<sup>[9,17,18]</sup> Electropolymerization has become a method of choice for environmentally friendly and controlled synthesis of polymeric materials, while also allowing the integration of a solar power generator for green energy production.<sup>[19]</sup> Meanwhile, other bioderived monomers with similar chemical structures to dopamine have also been electropolymerized. The formation of ultrathin films on conductive substrates such as gold as an additional layer providing groups for further functionalization is of emerging interest for fabricating biosensors, organic semiconductors, and new nanocomposite materials.<sup>[9,20–22]</sup> Polynorepinephrine (PNE), a structural analog of PDA,<sup>[23]</sup> is formed by polymerization of norepinephrine (NorEp) and has similar adhesive properties as that of PDA, but shows stronger hydrophilicity due to the additional aliphatic hydroxyl group of NorEp. This functional group also allows straightforward post-functionalization, which is challenging to achieve with polydopamine coatings.<sup>[23]</sup> To date, most studies on the electrodeposition of NorEp required preoxidation steps,<sup>[24,25]</sup> which renders this polymerization more complicated and limits the advantages of electropolymerization.<sup>[26,27]</sup> 3-Amino-L-tyrosine (ALT) represents another interesting monomer for the preparation of thin films. ALT is a synthetic derivative of L-tyrosine that may be enzymatically synthesized via a nitrotyrosine intermediate by reduction of the nitro group as depicted in **Scheme 1**.<sup>[28]</sup> It plays a role in the biosynthesis of the thermally sensitive chemiluminescent polymer diazo-luminomelanine, which is used in microwave dosimetry research.<sup>[29]</sup> Additionally, it has been copolymerized with dopamine to improve the electronic properties of PDA.<sup>[29,30]</sup> However, to our knowledge, electropolymerization of ALT has not been demonstrated yet.

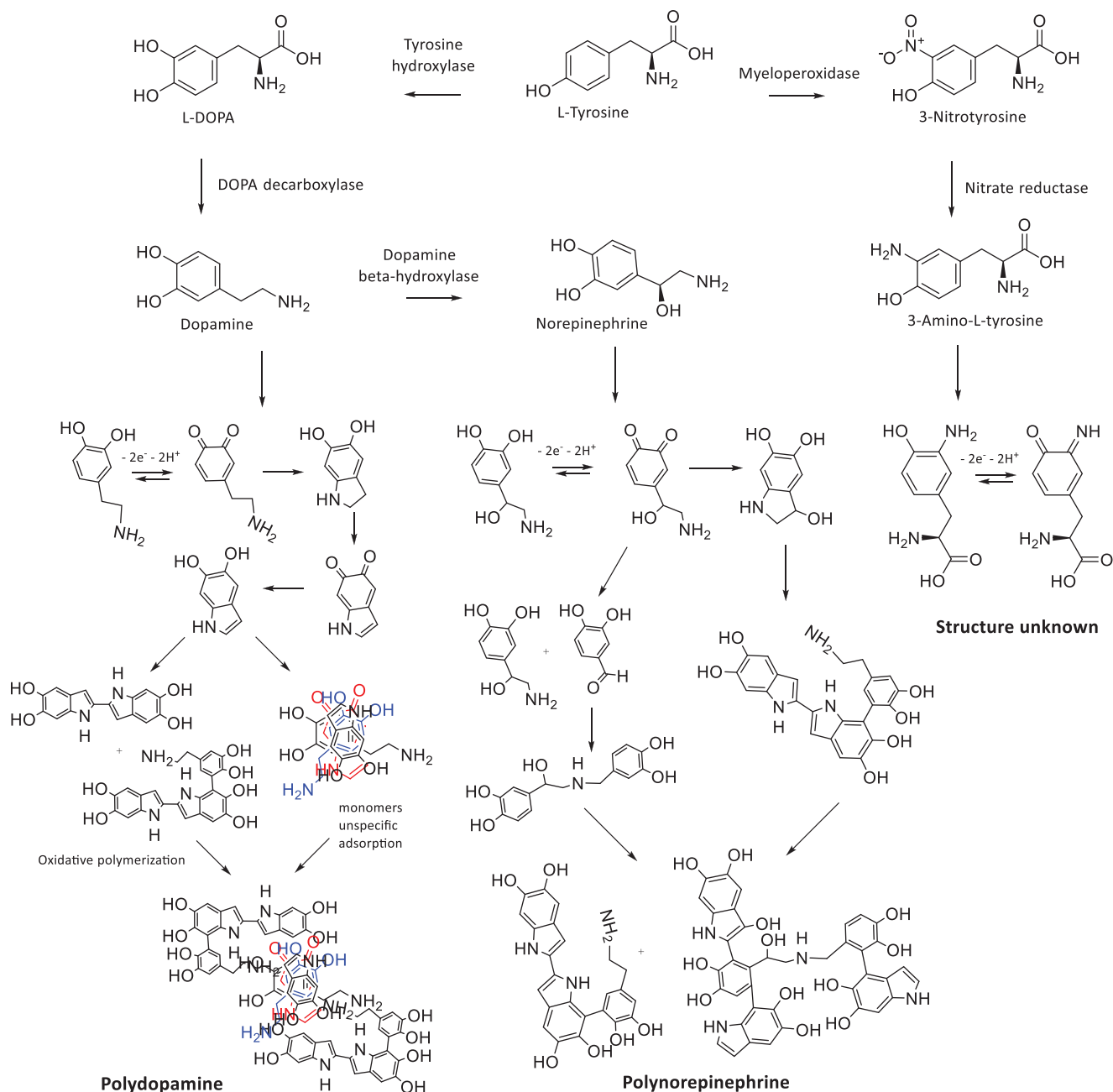
Herein, we report the electropolymerization of ALT to generate poly(amino-L-tyrosine) (PALT). Its characteristics such as film thickness, swelling behavior, surface roughness, and fluorescence quenching are compared with films made from PDA and the analogous PNE. We find that PALT affords ultrathin coatings whose thickness can be controlled at the low nanometer scale by the number of CV cycles. Furthermore, PALT produces films with remarkably smooth surfaces and exhibits much lower fluorescence quenching than PDA or PNE. Therefore, PALT films could be of great interest for the development of sensors and photoactive devices. Moreover, we demonstrate that PALT is readily degraded by hydrogen peroxide, making it a suitable candidate for complete green synthesis and disposal of polymeric materials.

## 2. Results and Discussion

The PALT thin films were prepared by electropolymerization using cyclic voltammetry and compared to PDA and PNE films, which have very similar cyclic voltammograms. For PDA and PNE, the upper and lower vertex potentials used were +0.5 and

−0.5 V, respectively (**Figure 1A,B**). In their cyclic voltammograms, an oxidation peak at +0.3 V was observed during the first electrochemical cycle, which corresponds to the oxidation of catechol to quinone. A reduction peak for the reverse reaction, quinone to catechol, appears at −0.3 V for PDA and −0.2 V for PNE. In both cases, the current decreases over each electropolymerization cycle until oxidation and reduction peaks can no longer be distinguished at the tenth cycle. This behavior indicates that the film, which is deposited during the cyclic voltammetry, is electrically insulating, as expected for both dopamine and norepinephrine monomers. Despite the similarities in the chemical structure of dopamine, NorEp, and ALT, the electropolymerization of ALT proceeds markedly different. Cyclic voltammetry of ALT using an upper vertex of +0.5 V revealed an oxidation peak at around 0.3 V (**Figure S1**, Supporting Information) but did not yield a robust film. Previous efforts to electropolymerize 2-aminophenol, a structurally similar molecule, also found that a film was not formed at lower potentials but that potentials as high as +1.2 V were required.<sup>[31–33]</sup> A second oxidation peak could then be observed around 0.8 V, which was attributed to the oxidation of the aromatic amino group, as schematically shown in **Figure S2** (Supporting Information). Therefore, the upper vertex for ALT was also increased to +1.2 V, while the lower vertex potential was kept at −0.5 V in order to facilitate oxidation of the amino group, leading to more efficient film formation. In the cyclic voltammogram of ALT presented in **Figure 1C**, a sharp phenol oxidation peak is observed at +0.3 V and a second oxidation peak occurs at +0.8 V, likely due to the oxidation of the amine present at the aromatic ring. In comparison to PDA and PNE, the decrease in current is less pronounced with each cycle, indicating the formation of a less insulating film. Mass deposition during the electropolymerization of all three monomers was tracked using electrochemical quartz crystal microbalance (eQCM) measurements. By monitoring the oscillation frequency of a gold-coated quartz crystal used as a working electrode, the deposition of the polymer at the electrode is observed as a decrease in the frequency of the crystal. For PDA and PNE, mass deposition is highest during the first four to five cycles and exhibits a continuous decrease in the deposition rate with further cycles, showing an asymptotic deposition rate over time (**Figure 1D**).

This behavior is in agreement with the results of the cyclic voltammetry experiments, where the current decreases rapidly in the first five cycles with smaller changes thereafter. Together, these data indicate an early, rapid deposition of insulating PDA or PNE oligomeric layers with the reduction in current on further cycling, limiting the later deposition. This observation is in line with previous reports that the electropolymerization of dopamine exhibits a self-limiting thickness.<sup>[16]</sup> Interestingly, for PALT, the deposition rate increases after the first three cycles, and it keeps growing even after the 14th cycle, suggesting the formation of a much less insulating film compared to PDA and PNE, as shown in **Figure 1D**. These features could also indicate the formation of a porous matrix, which does not inhibit the monomer diffusion to the electrode surface. The structure of polycatecholamines has not been fully elucidated yet, and the formed polymeric structures are likely affected by parameters such as the oxidation agent, buffer solution, and temperature at which the oxidative polymerization takes place.<sup>[34]</sup> These highly crosslinked polymeric materials are most likely composed of a



complex mixture of low-order oligomers of indole units held together by supramolecular interactions (Figure S3, Supporting Information).<sup>[35]</sup> In PDA and PNE, the long-range conjugated system is disrupted, which is responsible for their insulating or semiconductive characteristics. Until now, no film formation or no chemical structure has been reported for PALT. However, polymers based on 2-aminophenol have been analyzed, and phenoxazine ladder structures, depicted in Figure S4 (Supporting Information), were shown to be responsible for their conductive features.<sup>[31,32,36]</sup> Similar to 2-aminophenol, PALT films provide

increased conductivity compared to other polycatecholamines, which could be due to indole oligomerization and phenoxazine structure formation. The eQCM frequency changes with the number cycles and density of the deposited films can be derived using the Sauerbry equation (Equation (1)), where  $\Delta f$  is the frequency change due to mass deposition and  $C_f$  is a characteristic constant of the quartz crystal electrode. In combination with the thickness measured by atomic force microscopy (AFM), an estimation of the material density can be calculated since the Sauerbry equation used for the eQCM mass estimation

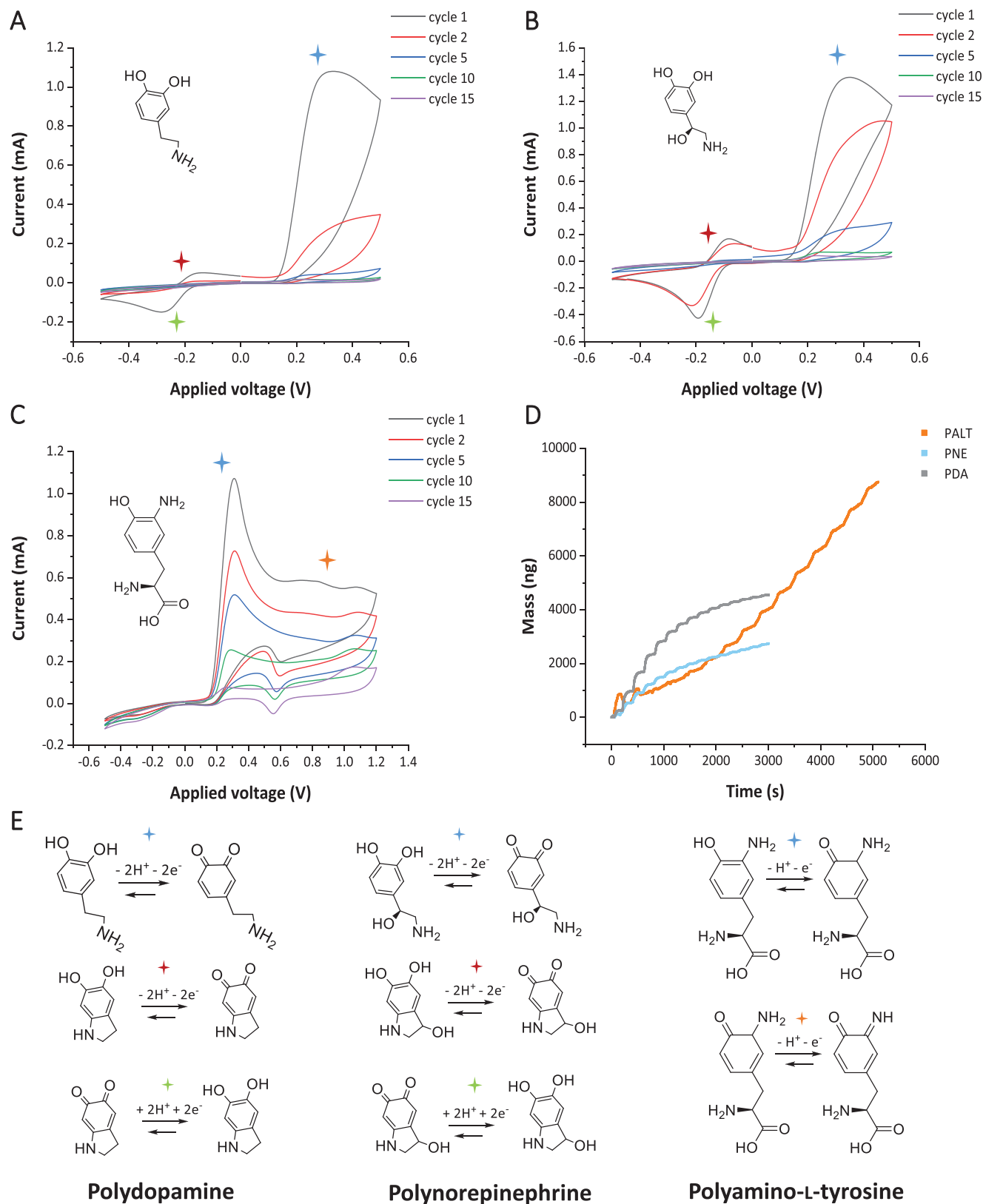


**Figure 1.** A–C) Cyclic voltammetry, D) eQCM data, and E) oxidation and reduction mechanisms of PDA, PNE, and PALT. A) PDA cyclic voltammetry shows an initial oxidation peak at 0.3 V attributed to the oxidation of catechol to quinone (blue star), a reduction peak (green star), and an oxidation peak (red star), attributed to the redox activity of leucodopaminechrome. B) PNE cyclic voltammetry reveals an initial oxidation peak at 0.3 V attributed to the oxidation of the catechol to quinone (blue star), a reduction peak (green star), and oxidation peaks (red star) attributed to the redox activity of

**Table 1.** Density of the films calculated from Equation (1).

Film	Density [g cm <sup>-3</sup> ]		
	5 cycles	10 cycles	15 cycles
PDA	1.79	1.91	1.75
PNE	1.66	1.43	1.41
PALT	1.43	1.52	1.38

assumes a uniform and compact film.<sup>[37]</sup> The results are listed in **Table 1**

$$-\Delta f = \Delta m \cdot C_f; C_f = 0.0815 \text{ Hz} \cdot \text{ng}^{-1} \cdot \text{cm}^{-2} \quad (1)$$

Unexpectedly high film densities<sup>[38]</sup> were obtained for all three polymers (Table 1), being highest for PDA. These high densities could be attributed to the electrochemical deposition process leading to the formation of particularly dense and homogeneous films, as previously discussed in literature.<sup>[39]</sup> For all polymeric films, the densities decrease after 15 cycles, possibly due to the deposition of a less well-packed material. This observation is more evident in the case of PALT, where a decrease from 1.52 g cm<sup>-3</sup> at 10 cycles to 1.38 g cm<sup>-3</sup> at 15 cycles was observed. For PNE, the density values decreased from the fifth to the tenth cycle while remaining almost constant thereafter. It is also worth considering that the assumptions at the base of the Sauerbry equation can lead to an overestimation of the film density, although the relative comparison between the different films remains valid. The thicknesses and morphologies of the deposited films were studied using AFM. In **Figure 2**, the microscopic images obtained from PDA, PNE, and PALT after ten electropolymerization cycles are shown. Overall, the films appear smooth and homogeneous. PDA and PNE show some nodules higher than 30 nm, and the number of nodules increases for higher numbers of electropolymerization cycles, suggesting multiple deposition mechanisms. Although some nodules are present, PNE appears to be comparatively smoother than PDA. On the other hand, PALT almost completely lacks nodules, indicating a uniform deposition mechanism. The film thickness for PNE and PDA increases almost linearly from 8.5 to 17 nm with increasing cycles. In contrast, the thickness of PALT films increases from 11 to 46 nm (Figure 2D) reaching a value three times higher than the other two films. These results are in line with eQCM data supporting the insulating behavior of PNE and the less insulating features of PALT. The surface roughness of both PNE and PALT exhibits a slight thickness-dependent increase, but it is still close to that of the gold electrode and considerably

lower than that of PDA as summarized in Table S1 (Supporting Information).

In addition to AFM, scanning electron microscopy (SEM) was used to characterize the surface morphology of the different films on gold. As depicted in Figure S5 (Supporting Information), the films show morphological changes with an increasing number of cycles. In particular, at five cycles, PDA still shows a surface similar to gold, while PNE and PALT seem to better cover the original morphology. Upon increasing the number of cycles, both PDA and PNE increase in roughness showing the formation of nodules that render the surface less homogeneous. It is likely that such nodules arise for two main reasons: the tendency of catecholamine to self-polymerize when the concentration of reacted monomer at the electrode surface increases, and the lower electron transfer due to the insulating property of the films, which makes the electrodeposition less efficient in favor of a more random polymer deposition on the surface. Interestingly, PALT does not show the same trend, and the polymeric film appears more homogeneous for higher the numbers of cycles. In order to gain more information on the chemical structure of the resultant PALT, PDA, and PNE films, X-ray photoelectron spectroscopy (XPS) was performed. XPS signatures from C, N, and O were obtained from high-resolution spectra for all films after ten cycles of electrochemical deposition<sup>[40,41]</sup> (Figure S6, Supporting Information). The area percentages, which indicate the abundance of the different functional groups in the films, are summarized in **Table 2**. PDA and PNE show similar percentage values for C 1s spectra indicating similarity in the final polymeric structure. Compared to PDA, PNE reveals a similar distribution in the amine and amide groups but a higher content of hydroxyl groups, most likely due to the additional aliphatic hydroxyl group of NorEp. On the other hand, PALT reveals a much higher percentage corresponding to the carbonyl group, possibly originating from condensed carboxylic acid products in PALT molecule.

Next, changes in the composition of the soluble fraction of intermediates formed during electropolymerization were investigated using in situ UV-vis spectroscopy. PNE and PDA exhibit similar changes in their spectra over the course of the electropolymerization process (**Figure 3**). Initially, peaks around 300 and 480 nm are observed, similar to the autoxidation of catecholamines, due to the presence of aminochrome-like structures formed from the initial oxidation and cyclization of the catecholamines.<sup>[42]</sup> Later, a continuous increase in the absorbance across the visible spectrum is seen due to further oligomeric and polymeric species.<sup>[42,43]</sup> The spectra of PALT electropolymerization, on the other hand, indicate a different mechanism (Figure 3). The spectra are dominated by overlapping peaks centered at 340 nm, attributed to the conjugation of two ALT monomers, and at 430 nm, which have been attributed to the formation of phenoxazine structures in the oxidation

aminochrome structures and benzaldehydes that are shown at -0.2 and -0.1 V, respectively. C) PALT cyclic voltammogram with oxidation peaks from the aromatic hydroxyl group (blue star) and amino group (orange star) at +0.3 and +0.8 V, respectively. The current decreases rapidly with each cycle for PDA and PNE due to the formation of an insulating polymeric film. PALT exhibits a smaller decrease in current suggesting the formation of a less insulating film. D) eQCM mass deposition over time is represented by indicating an asymptotic deposition behavior from PDA and PNE, while PALT reveals an unusual increase in the film deposition rate. E) The oxidation and reduction mechanisms for each peak in the cyclic voltammogram are depicted. For PDA and PNE, three redox reactions are noticeable: oxidation of catechol to quinone of the monomer as a first peak (blue star), oxidation and reduction of the intracyclic form aminochrome (red and green stars, respectively). For PALT, only the two initial oxidation steps are recognizable, attributed to the oxidation of the hydroxyl group (blue star) and the amino group (red star).



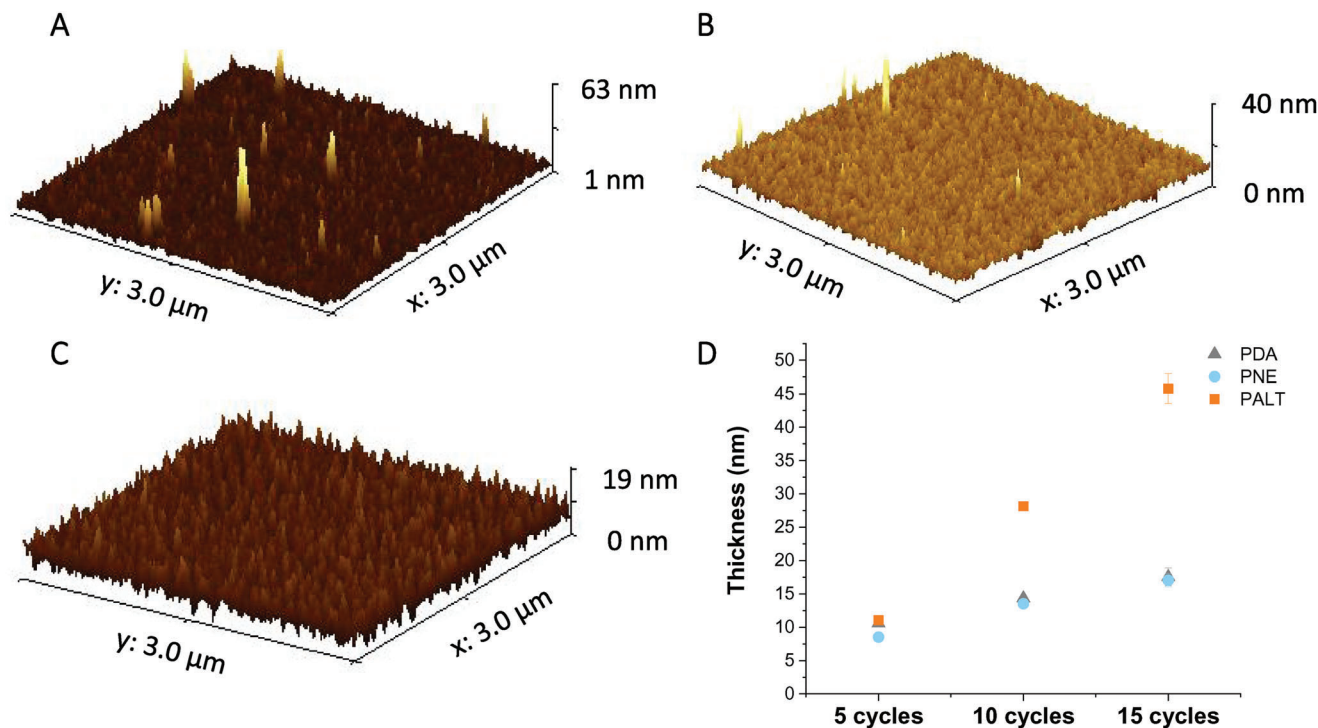


**Figure 2.** A–C) AFM image of ten cycles electrodeposited films on gold of PDA, PNE, and PALT, respectively. D) Thickness dependence on the number of cycles for the three different polymeric films. The thickness was determined by scratching the film on gold using a plastic tip and measuring the step using AFM.

**Table 2.** Area percentages of the different functional group contributions calculated from high-resolution XPS spectra of PDA, PNE, and PALT films prepared by electropolymerization. The fitted spectra are shown in Figure S6 (Supporting Information).

Elements	Functional groups	PDA [%]	PNE [%]	PALT [%]
C 1s	C–C	44.3	41.6	40.1
	C–OH	46.5	47.9	43.8
	C=O	9.2	10.5	15.9
O 1s	C–OH	54	78.6	76.3
	C=O	46	21.4	23.6
N 1s	R <sub>2</sub> –NH	52.3	50.9	37.6
	R–NH <sub>2</sub>	28.3	33.7	17.8
	RN=	19.4	15.4	44.5

of aminophenol.<sup>[44,45]</sup> Similar to poly(aminophenol) formation, phenoxazine structures could, in principle, serve as new monomers during the formation of PALT resulting in different polymeric structures compared to PNE and PDA.<sup>[31–33]</sup>

In order to obtain a more comprehensive chemical analysis of the synthesized films, the Fourier transform infrared (FTIR) spectra of all three polymer coatings after ten cycles were recorded and are depicted in Figure S7 (Supporting Information). All three films show polymeric broadband absorbance at around 3500 and at 1600 cm<sup>-1</sup> with a few appreciable differences in the finger print region. Next, the electrodes with the coated films were characterized by electrochemical impedance spectroscopy

(EIS), using a 5 mM solution of potassium ferrocyanide in phosphate buffer pH 7 as a redox probe in the frequency range between 0.01 and 10<sup>5</sup> Hz. In EIS, the resistance to electron transfer is represented by the semicircle diameter in the Nyquist plot<sup>[46,47]</sup> (Figure 4). The gold surface with the deposited film was characterized for 5 and 15 cycles of deposition. The data were fitted with a Randle equivalent circuit formed by a resistance, attributed to the solution ( $R_s$ ), in series with a resistance and a constant phase element placed in parallel to extract the resistance to charge transfer ( $R_{ct}$ ), as shown in Figure 4. In the case of PDA and PNE, the data could be fitted from 100 kHz to 0.01 Hz, while for PALT this was not possible since the samples were likely undergoing changes during the measurements. For this reason, the fitting of the experimental values for PALT was performed considering the portion of data up to 0.1 Hz, where the material was mostly stable. In this region, the measurements conformed to the Kramers–Kronig test, which correlates the real and imaginary parts of the spectrum to a system that is linear, casual, and invariant with time. These data are fitted with a sufficiently general model built as a resistor in series with a number ( $N$ ) of RC elements to estimate the final validity. As expected, the resistance to charge transfer derived from the film increased rapidly with higher deposition cycles and film thickness, as shown previously.<sup>[26,34]</sup> PALT exhibited the lowest resistance while also forming the thickest films suggesting the formation of a less compact structure compared to PDA and PNE, thus supporting the results of the density measurements. However, another explanation for these observations could be that the PALT film is permeable to ions. Over three consecutive measurements on the same sample,

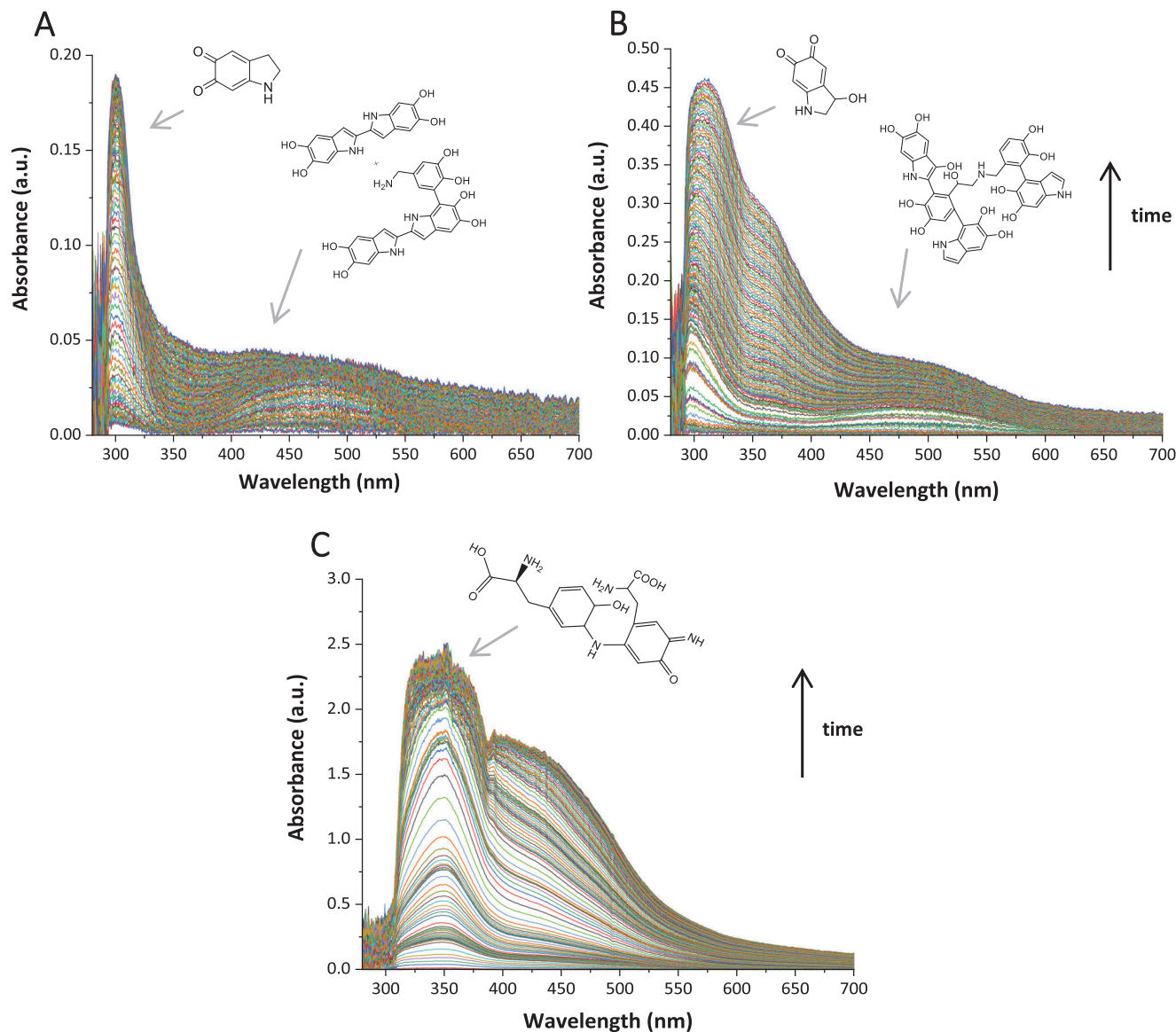


**Figure 3.** In situ UV-vis absorbance for A) PDA, B) PNE, and C) PALT during 15 cycles of CV. Possible oxidation products and oligomers are inserted in correspondence to the respective absorbance peak.

the resistance to charge transfer decreased in the high-frequency range of the impedance spectrum. Contrary, in the low-frequency region, the resistance is substituted by a straight line indicating a resistance to mass transfer, known as Warburg resistance. The observed phenomena would suggest that the PALT film is composed of a porous structure that can absorb the electrolyte over time, allowing free movements of ions, thereby exhibiting reduced resistance. The behavior was studied in several samples, and the values of  $R_{ct}$  extracted from the fit are plotted in Figure S8 (Supporting Information). Moreover, the observation agrees with the different deposition rates depicted by eQCM experiments. Among the three polycatecholamines studied, PDA shows the highest resistance when deposited with only 5 cycles while PNE reveals the same behavior as PDA after 15 cycles of deposition confirming the formation of a homogeneous and insulating poly-

mer coating. EIS measurements have a low temporal resolution hence preventing detailed studies of changes occurring in the films over time. Therefore, we employed a surface plasmon resonance (SPR) technique to further investigate and monitor the apparent swelling phenomena of the films, which was particularly prominent for PALT. The shift originating from the resonance dip in the SPR spectra was monitored over time in order to prove the swelling behavior. The SPR signal shifted to lower wavelengths over time after immersion of the substrate in water (Figure 4E), which was attributed to the permeation of water into the matrix, resulting in an increase of porosity and decrease of optical density.

The shift was noticeable only for the PALT matrix while PDA and PNE did not show significant changes over time, as shown in Figure 4E, as expected from the impedance measurements.

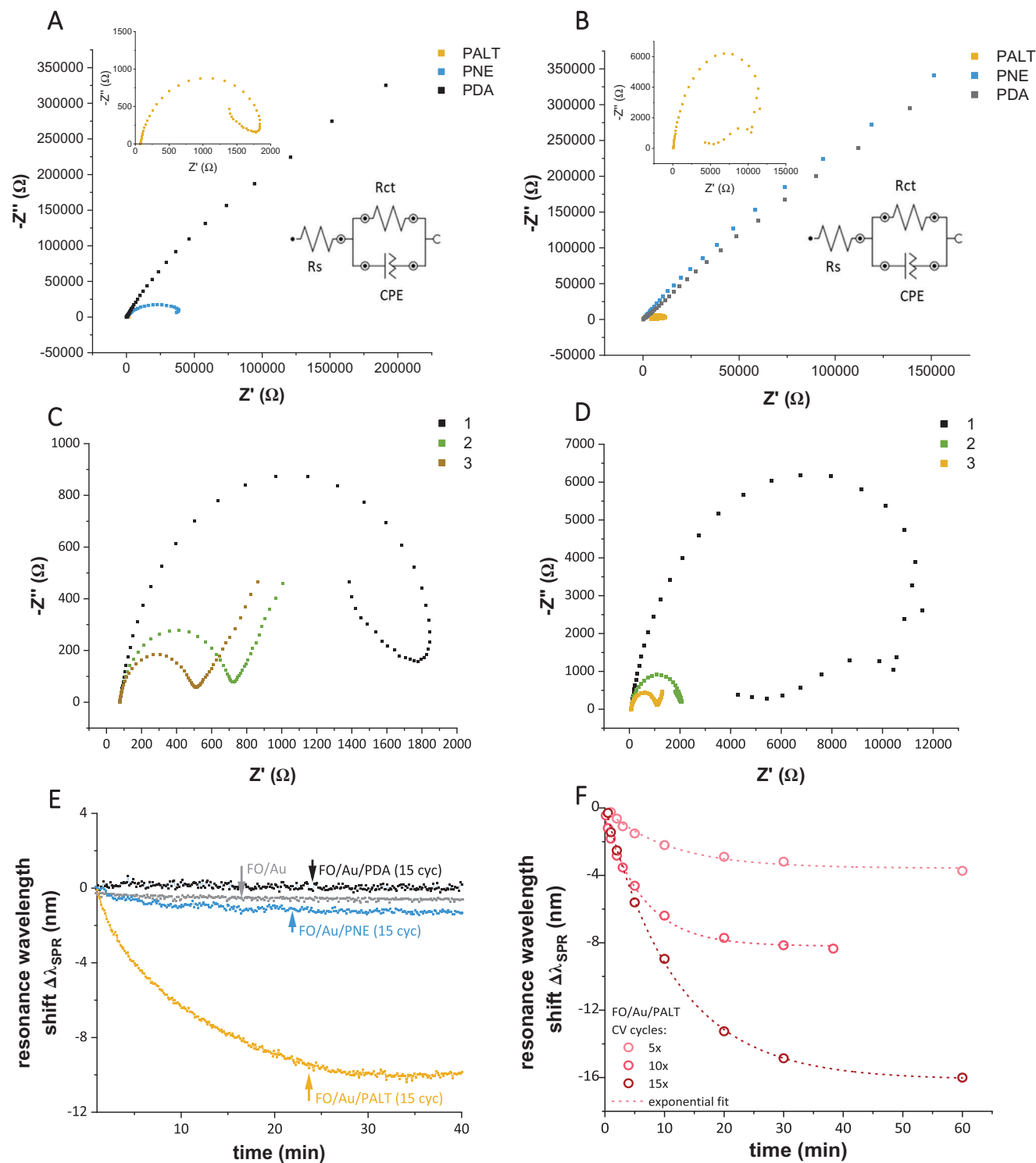


**Figure 4.** Electrochemical impedance spectroscopy data for PDA, PALT, and PNE. A) 5 cycles and B) 15 cycles. Inset: Magnification of the PALT region. C) Impedance spectroscopy of PALT five cycles and D) PALT 15 cycles with repetitively being performed on the same samples to show the progressive decreasing of impedance over three times of repetitive measurements. E) Shift in wavelength of the resonance dip for the three different materials at the higher thickness. F) Resonance wavelength shift for the three different thicknesses of ALT film, showing an exponential decay.



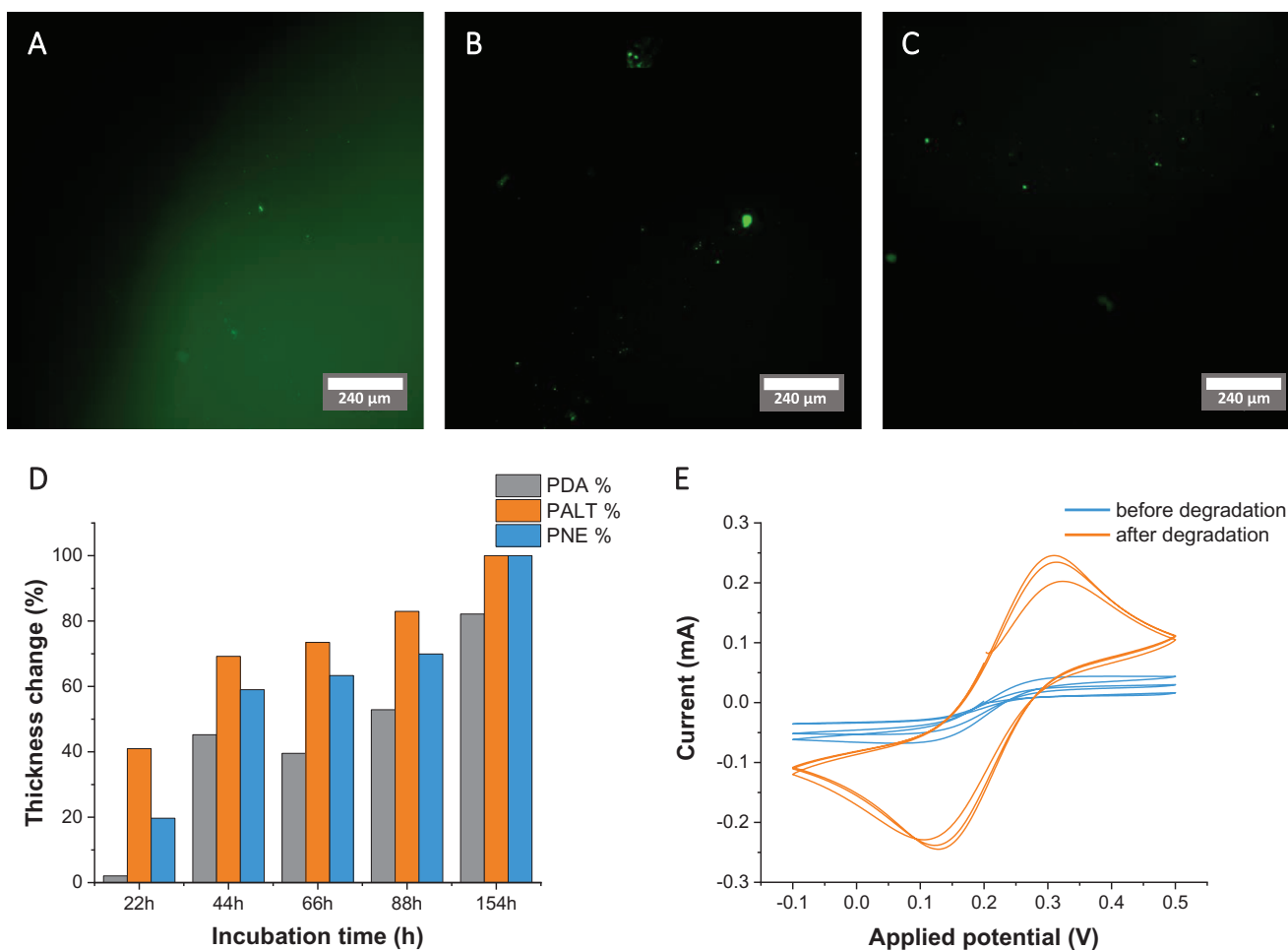


**Figure 5.** Fluorescence images of A) PALT, B) PNE, and C) PDA after overnight incubation with 1 mg mL<sup>-1</sup> FITC. Images were taken through a 10× objective using an FITC filter set. Scale bar = 240 μm. D) Percentage of the thickness change for films made from five cycles of PALT, ten cycles of PNE, and ten cycles of PDA after incubation in H<sub>2</sub>O<sub>2</sub> 50 mM for 154 h. E) Example of K<sub>3</sub>[Fe(CN)<sub>6</sub>]/K<sub>4</sub>[Fe(CN)<sub>6</sub>] CV on PALT film before and after degradation study; the CVs of PNE and PDA after the degradation study are shown in Figure S11 (Supporting Information).

More investigations were carried out to compare the three film thicknesses for the PALT matrix (5, 10, and 15 cycles); the data clearly show a drift attributed to swelling for all three thicknesses. In addition, an increase of the drift signal proportional to the thickness of the sample is observed. The data could also be fitted with an exponential decay function reaching a steady state after 30, 40, and 60 min of immersion for 5, 10, and 15 cycles, respectively. The SPR data supported the behavior that was initially observed by impedance spectroscopy, confirming that the ALT electropolymerization affords a porous film. These porous materials allow solvent infiltration together with the ions present in the solution, thereby resulting in an electrochemical resistance lower than expected for films of similar thickness. In addition to these unexpected physical features, it can be predicted that ALT presents different photophysical properties compared to polycatecholamines. Polycatecholamines such as PDA are known to be potent fluorescence quenchers,<sup>[48–50]</sup> which make them unsuitable for some applications where fluorescence is important, such as chromophore-based sensors and reporters.<sup>[51]</sup> The quenching behavior is attributed to the nanos-

structure of PDA possessing a high degree of  $\pi$ - $\pi$  interactions and to the presence of the catechol moiety.<sup>[51]</sup> By introducing phenoxazine structural units, PALT is expected to have a different nanostructure to that of other polycatecholamines and thereby may have a lower degree of quenching. To determine the relative quenching effect, each film was incubated overnight with a 1 mg mL<sup>-1</sup> solution of fluorescein isothiocyanate (FITC) solution in phosphate buffer pH 8.5, restrained to a 3 mm diameter area of the film using a polydimethylsiloxane (PDMS) mask (Figure S9, Supporting Information). After washing and incubation in a pure phosphate buffer (pH 7.0) for 72 h, the films were imaged on an epifluorescence microscope. It can be clearly observed that FITC-treated PALT exhibits a significantly higher fluorescence than PNE and PDA (Figure 5A–C) suggesting that it is a less potent quencher. Therefore, for applications using fluorescence reporters, PALT is better suited than PNE and PDA. To evaluate the degradability of the films, the effect on the film integrity by the incubation in 50 mM H<sub>2</sub>O<sub>2</sub> in water was investigated. Each film was freshly prepared on gold, and the thickness was determined before and after the incubation with an

AFM microscopic image (Figure S10, Supporting Information) obtained by carefully scratching the film with a plastic tip. The CV of  $K_3[Fe(CN)_6]/K_4[Fe(CN)_6]$  was also recorded before and after incubation.

The relative change in thickness is shown in Figure 5D. A dramatic change in thickness appears after 24 h incubation for PNE and PALT films, while for PDA a significant change is noticed after 44 h, indicating superior chemical stability of the PDA. Moreover, all the films show a remarkable decrease in the peak current when performing potassium ferro-/ferricyanide cyclic voltammetry, which was completely recovered after degradation of the films, confirming the degradation and complete removal of the film from the conductive surface as shown in Figure 5E, using oxidative conditions. Although polycatecholamine films have been shown to be highly stable in both aqueous and organic solvents,<sup>[41]</sup> the observed degradation of the films in a relatively low-concentration solution of  $H_2O_2$  opens the possibility of selective degradation of films. This is an important property for end-of-life water reduction. In particular, at low concentrations,  $H_2O_2$  is an environmentally friendly oxidizer that can even be directly generated by some enzymes such as glucose oxidase, thereby providing a fully green process.

### 3. Conclusion

Herein, the electrodeposition of two bioderived analogs of dopamine was successfully demonstrated and analyzed. The preparation of the new ultrathin polymer film PALT was accomplished for the first time using electropolymerization of the monomer 3-amino-L-tyrosine, and its properties were compared to the known polymers PDA and PNE. The chemical and physical properties of these films were characterized in detail using a combination of in situ techniques, such as eQCM, spectro-electrochemistry, and EIS, and standard techniques such as FTIR, AFM, and XPS. PNE shows similar behavior to PDA, both in electrochemical preparation with similar oxidation and reduction peaks and in quenching properties, a well-known characteristic for polycatecholamines. However, despite its structural similarity to catecholamine, PALT films provide different features such as nonlimited deposition during the preparation at the electrode and a significant reduction in quenching capacity. These characteristics, together with the low impedance observed in EIS measurements, highlight the potential usage of this polymer as nanocomposite materials for the preparation of biosensing surfaces, where a low electrical resistance is desirable,<sup>[52]</sup> or the integration of photoactive inorganic particles like quantum dots or nanorods for applications that rely upon fluorescence or light interactions, e.g., as sensors or in photocatalysis. We also demonstrated the complete degradation of the PALT films under mild oxidative conditions, enabling cradle-to-grave bioprocessing of these films. In addition, the very smooth surface together with the possibility of controlling the film thickness makes it suitable for the preparation of biosensors via immobilization of DNA aptamers or peptides. Our results contribute to green material technologies based on the electrodeposition of polymer films that could be prepared using sunlight in the future and that are degradable by enzymes.

### 4. Experimental Section

**Materials:** Gold-coated (1000 Å) microscope slides (Sigma-Aldrich) were cut using a diamond tip. Phosphate buffer (pH 7, 100 mM) was prepared, using sodium phosphate dibasic anhydrous (99%) and sodium phosphate monobasic (99%) (Sigma-Aldrich), in Milli-Q water. Carbonate buffer (pH 10, 100 mM) was prepared, using sodium bicarbonate (>99.7%) and sodium carbonate (>99.8%) from Sigma-Aldrich, in Milli-Q water. Gold-coated quartz crystals (6 MHz) (Metrohm) were used for electrochemical quartz crystal microbalance measurements. Potassium ferricyanide (99+%) and potassium ferrocyanide trihydrate (99+%) were obtained from Acros Organics. Sodium dihydrogen phosphate was obtained from Sigma-Aldrich and potassium hydrogen phosphate from Appli Chem.

**Electropolymerization of the Polymeric Films:** Electropolymerization and cyclic voltammetry experiments were performed analog to the previous work<sup>[53]</sup> using a Metrohm Autolab N series potentiostat (AUTOLAB PGSTAT 204) with a standard three-electrode configuration. A gold-covered glass microscope slide was used as the working electrode, Ag/AgCl, 3 M KCl as the reference electrode, and a gold wire as the counter electrode for film preparation, while a platinum wire was used as counter electrode for electrochemical impedance spectroscopy experiments. All reactions were performed in a 35 mL electrochemical cell (Metrohm), under air atmosphere and at room temperature. Pretreatment of the gold working electrode was performed by Ar plasma cleaning for 10 min at 6 mbar pressure. Gold was used as a substrate for electrodeposition of films due to its inertness, excellent conductivity, and low surface roughness.

**Electropolymerization of PDA and PNE Films:** The gold substrate was immersed in a solution of monomer (dopamine hydrochloride, norepinephrine, or amino-L-tyrosine; 1 mg mL<sup>-1</sup>) dissolved in 100 mM phosphate buffer at pH 7.0. A potential was applied and cycled from +500 to -500 mV for PDA and PNE, while from +1200 to -500 mV was used for ALT to induce polymerization at the interface. The scan rate was 0.01 V s<sup>-1</sup> in all the three cases.

**eQCM Characterization of the Polymer Films:** An electrochemical quartz crystal microbalance measurement was conducted in a 3 mL electrochemical cell using Ag/AgCl reference electrode and gold counter electrode, by minimizing the driving force prior starting the measurement.

**Spectro-Electrochemistry:** All reactions were performed in a standard quartz cuvette electrochemical cell placed in a cuvette holder ported for fiber optic (FO) connectors on three sides. As described above, a three-electrode setup was used with a gold-coated microscope slide as the working electrode, a gold wire as the counter electrode, and Ag/AgCl as the reference electrode. In addition, the light from a deuterium and halogen lamp was passed through the reaction solution directly in front of the working electrode via fiber optic connection and the transmitted light collected by a spectrophotometer. The electropolymerization was performed under air atmosphere and at room temperature. Pretreatment of the gold working electrode was performed by in Ar plasma cleaning for 10 min at a pressure of 6 mbar. The same procedure described above was used for each respective monomer. Absorbance was calculated using the initial spectrum for each solution (immediately before the beginning of electropolymerization) as reference.

**Electrochemical Impedance Spectroscopy:** Electrochemical impedance spectroscopy was conducted on 1 cm<sup>2</sup> coated electrode surface using a 5 mM solution of equimolar  $K_3[Fe(CN)_6]/K_4[Fe(CN)_6]$  in phosphate buffer (pH 7, 100 mM 1.5 mL) confining the analyzed area with an O-ring of 8 mm in diameter. As a counter electrode, a Pt wire was used; the applied potential was 0.2 V against Ag/AgCl reference electrode with an amplitude of 0.01 V and applying a frequency from 0.01 to 10<sup>5</sup> Hz.

**Atomic Force Microscopy:** Atomic force microscopy was used to physically characterize the film, measure the morphology, surface roughness, and thickness of the polymer films on gold by scratching it with a plastic tip after it was freshly prepared. The profile of the scratch was then recorded by AFM (Park NX20 and Bruker Dimension ICON) with a cantilever 70 kHz resonance frequency and an elastic constant of 2 N m<sup>-1</sup>.

**Scanning Electron Microscopy:** Scanning electron microscopy was used to physically characterize the films, imaging the surface morphology

of the films prepared on gold. The images were recorded by SEM (Hitachi SU8000) using a working distance of  $\approx 2000\ \mu\text{m}$  and at a magnification of 50 000 with an acceleration voltage of 1600 V and a deceleration voltage of 1500 V.

**Fourier Transform Infrared Spectroscopy:** The infrared spectra of the film on gold were obtained by grazing-angle reflectance FTIR (Vertex 70, Bruker) after purging the sample with dry air for 15 min and recording four spectra at 3000 scans with an interval of 1 min between each one.

**X-Ray Photoelectron Spectroscopy:** XPS was conducted using a Kratos Axis UltraDL spectrometer 3 (Kratos, Manchester, England) using an Al K excitation source with a photon energy of 1487 eV. The data were acquired in the hybrid mode using a  $0^\circ$  take-off angle, defined as the angle between the surface normal and the axis of the analyzer lens. Detailed region XPS spectra were collected with setting the analyzer pass energy at 80 eV, and a linear background was subtracted for all peak quantifications. The peak areas were normalized by the manufacturer-supplied sensitivity factors, and surface concentrations were calculated using CasaXPS software. N 1s, C 1s, and O 1s high-resolution spectra were collected with an analyzer pass energy of 20 eV. A neutralizer was always used during spectra collection.

**Fabrication of Gold-Coated Optical Fiber Substrates:** Plasmonic FO probes were prepared according to previously reported procedures.<sup>[54]</sup> Tips of 6.5 cm in length were cut from Technology Enhanced Clad Silica (TECS-clad) multimode optical fiber cable (Thorlabs) with a numeric aperture of 0.39 and a core diameter of  $1000\ \mu\text{m}$ . At one end of the tip, an optically active section for SPR was constructed by removing the outer jacket layer with a dedicated mechanical stripping tool and subsequent dissolution of the inner polymer cladding with acetone. Obtained tips were cleaned with Milli-Q water and isopropanol, and blow-dried with compressed air before coating them homogeneously with 50 nm of gold in an EM ACE600 sputter coater (Leica Microsystems) using a sputter rate of  $0.11\ \text{nm s}^{-1}$  on a rotating stage. As-sputtered FO tips were further thermally annealed at  $180\ ^\circ\text{C}$  for 7 h according to a previously reported procedure.<sup>[55]</sup> As reported, mild thermal treatment resulted in a morphological change associated with a grain growth of the vacuum-deposited gold layer. This ensured a better stability of the Au film during the electropolymerization step and blueshifted the plasmonic signal, leading to a larger operational window for polymer films with a higher refractive index. To ensure a good electrical connection across the transition of the upper gold-coated part of the fiber to the thinner optical active section, conductive silver paint (Ag-paint, RS Components, Ltd.) was applied and dried at room temperature for 2 h. To avoid a possible influence of the silver coating, this section was further coated by applying a liquid heat shrink tubing (Performix Liquid Tape, Plastidip, Plasti Dip Europe GmbH) and dried at room temperature for 16 h. As-prepared FO probes were stored under argon until further usage.

**FO-SPR Measurements:** FO probes were connected to a Y-optical splitter ( $400\ \mu\text{m}$  core diameter, and a numeric aperture of 0.39, Thorlabs) with a commercially available bare fiber terminator (Thorlabs) via a SMA905 connection. Polychromatic light (quartz tungsten-halogen lamp, 400–2200 nm, 50 mW, Thorlabs) was focused with an achromatic lens (Thorlabs) on the backend of an input arm of the Y-optical splitter and guided to the tip of the plasmonic fiber probe in order to resonantly excite propagating surface plasmons on its lateral gold surface. The light was backreflected at the gold-coated cross section of the tip and collected in a spectrometer (HR4000CG-UV-NIR, OceanOptics, Inc.), connected to the output arm of the Y-optical splitter. The measured backreflected spectrum was normalized with that of the tip in air. In the case of PALT-coated fiber tips, the reference spectra of a gold-coated FO tip in air (without polymer layer) were used, because the high refractive index of PALT would lead to a plasmonic feature in the detectable range of the reference spectra recorded in air. FO probes were then dipped into Milli-Q water, and normalized reflectivity spectra were recorded. The acquisition time of the spectrometer was set to 5 ms, and 100 spectra were averaged per measurement point. The minimum position of the plasmonic dip (resonance wavelength  $\lambda_{\text{SPR}}$ ) in the normalized reflectivity spectra was fitted and tracked over time using a dedicated LabVIEW software.<sup>[56,57]</sup>

**Fluorescence Studies:** A PDMS mask with a 3 mm diameter hole was placed on the surface of each film.  $10\ \mu\text{L}$  of a  $1\ \text{mg mL}^{-1}$  solution of FITC in

100 mM phosphate buffer (pH 8.5) was introduced into the hole and incubated overnight at room temperature. The next day, each film was washed with phosphate buffer (pH 7.0) and Milli-Q water, then incubated for 72 h in a pure phosphate buffer (pH 7.0) to remove unbound FITC. A new phosphate buffer (pH 7.0) was added to the films, and they were imaged on an epifluorescence microscope using an FITC filter set. A  $10\times$  objective was used.

**Degradation Studies:** Oxidative degradation of the polymeric films in  $\text{H}_2\text{O}_2$  was investigated by incubating the films for four intervals of 22 h and one interval of 3 days in 9 mL of a 50 mM solution of  $\text{H}_2\text{O}_2$  in Milli-Q water at room temperature. The degree of degradation was investigated by AFM, by measuring the changes in the depth profile at every interval and by cyclic voltammetry of  $\text{K}_3[\text{Fe}(\text{CN})_6]/\text{K}_4[\text{Fe}(\text{CN})_6]$  before and after the degradation experiment.

## Supporting Information

Supporting Information is available from the Wiley Online Library or from the author.

## Acknowledgements

The authors acknowledge Christopher Ender, Marcel Boecker, and Dr. David Ng for helpful scientific discussions. In addition, the authors thank Gunnar Glasser for performing the SEM images of the films. The authors acknowledge support by the Deutsche Forschungsgemeinschaft (DFG, German Research Foundation) under the Collaborative Research Center (CRC) Transregio 234 (Grant Nos. 364549901, B04). This project has received funding from the European Union's Horizon 2020 research and innovation program under the Marie Curie Skłodowska-Curie grant agreement No 813863 BORGES. Open Access funding provided by the Max Planck Society was acknowledged.

Open access funding enabled and organized by Projekt DEAL.

## Conflict of Interest

The authors declare no conflict of interest.

## Author Contributions

T.M.D. and S.H. prepared the samples, optimized the procedures, analyzed the data, and wrote the manuscript. S.S. and J.M. helped with the sample preparation. R.H. performed the optic fiber SPR experiments and W.K. supervised and supported the SPR studies. C.V.S. corrected the manuscript and helped with the scientific discussion throughout the project. S.H. supervised the project. T.W. supported and supervised the whole project, helped with scientific discussion, and with writing the manuscript. The manuscript was written through contributions of all authors. All authors have given their approval to the final version of the manuscript.

## Data Availability Statement

The data that support the findings of this study are openly available in Zenodo repository at <https://doi.org/10.5281/zenodo.6579333>.

## Keywords

biodegradable polymeric films, bioinspired bioderived polymeric films, electrodeposition, green polymer chemistry, poly(amino-L-tyrosine), lypnorepinephrine

Received: April 7, 2022

Revised: May 25, 2022

Published online: July 1, 2022

- [1] A. Gandini, T. M. Lacerda, *Prog. Polym. Sci.* **2015**, *48*, 1.
- [2] Y. Zhu, C. Romain, C. K. Williams, *Nature* **2016**, *540*, 354.
- [3] R. Mülhaupt, *Macromol. Chem. Phys.* **2013**, *214*, 159.
- [4] M. A. Rahim, S. L. Kristufek, S. Pan, J. J. Richardson, F. Caruso, *Angew. Chem., Int. Ed.* **2019**, *58*, 1904.
- [5] T. S. Sileika, D. G. Barrett, R. Zhang, K. H. A. Lau, P. B. Messersmith, *Angew. Chem., Int. Ed.* **2013**, *52*, 10766.
- [6] B. Lochab, S. Shukla, I. K. Varma, *RSC Adv.* **2014**, *4*, 21712.
- [7] J.-J. Xu, X. Fang, C.-Y. Li, L. Yang, X.-Y. Chen, *aBIOTECH* **2020**, *1*, 97.
- [8] T. Fukuoka, Y. Tachibana, H. Tonami, H. Uyama, S. Kobayashi, *Biomacromolecules* **2002**, *3*, 768.
- [9] P. Salazar, M. Martín, J. L. González-Mora, *Polym. Sci. Res. Adv. Prat. Appl. Educ. Asp.* **2007**, *1*, 385.
- [10] S. Li, H. Wang, M. Young, F. Xu, G. Cheng, H. Cong, *Langmuir* **2019**, *35*, 1119.
- [11] H. Lee, S. M. Dellatore, W. M. Miller, P. B. Messersmith, *Science* **2007**, *318*, 426.
- [12] D. Chen, Y. Mei, W. Hu, C. M. Li, *Talanta* **2018**, *182*, 470.
- [13] H. Zhang, J. Luo, S. Li, Y. Wei, Y. Wan, *Langmuir* **2018**, *34*, 2585.
- [14] H. Guo, Z. Yao, J. Wang, Z. Yang, X. Ma, C. Y. Tang, *J. Membr. Sci.* **2018**, *551*, 234.
- [15] S. Daboss, J. Lin, M. Godejohann, C. Kranz, *Anal. Chem.* **2020**, *92*, 8404.
- [16] B. Stöckle, D. Y. W. Ng, C. Meier, T. Paust, F. Bischoff, T. Diemant, R. J. Behm, K.-E. Gottschalk, U. Ziener, T. Weil, *Macromol. Symp.* **2014**, *346*, 73.
- [17] L. E. Aguilar, B. Tumurbaatar, A. Ghavaminejad, C. H. Park, C. S. Kim, *Sci. Rep.* **2017**, *7*, 9432.
- [18] S. Kim, L. K. Jang, H. S. Park, J. Y. Lee, *Sci. Rep.* **2016**, *6*, 30475.
- [19] M. Garedew, C. H. Lam, L. Petitjean, S. Huang, B. Song, F. Lin, J. E. Jackson, C. M. Saffron, P. T. Anastas, *Green Chem.* **2021**, *23*, 2868.
- [20] V. Baldoneschi, P. Palladino, S. Scarano, M. Minunni, *Anal. Bioanal. Chem.* **2020**, *412*, 5945.
- [21] G. Loget, J. B. Wood, K. Cho, A. R. Halpern, R. M. Corn, *Anal. Chem.* **2013**, *85*, 9991.
- [22] J. H. Kim, M. Lee, C. B. Park, *Angew. Chem., Int. Ed.* **2014**, *53*, 6364.
- [23] M. K. Sung, J. Rho, I. S. Choi, P. B. Messersmith, H. Lee, *J. Am. Chem. Soc.* **2009**, *131*, 2145.
- [24] Y. Liu, X. Nan, W. Shi, X. Liu, Z. He, Y. Sun, D. Ge, *RSC Adv.* **2019**, *9*, 16439.
- [25] S. Khetani, V. O. Kollath, E. Eastick, C. Debert, A. Sen, K. Karan, A. Sanati-Nezhad, *Biosens. Bioelectron.* **2019**, *145*, 111715.
- [26] F. Bernsmann, J.-C. Voegel, V. Ball, *Electrochim. Acta* **2011**, *56*, 3914.
- [27] J. Vatrál, R. Boča, W. Linert, *Monatsh. Chem.* **2015**, *146*, 1799.
- [28] H. R. Gerding, C. Karreman, A. Daiber, J. Delp, D. Hammler, M. Mex, S. Schildknecht, M. Leist, *Redox Biol.* **2019**, *26*, 101251.
- [29] J. G. Bruno, J. L. Kiel, *Bioelectromagnetics* **1994**, *15*, 315.
- [30] M. Ambrico, P. F. Ambrico, A. Cardone, N. F. Della Vecchia, T. Ligonzo, S. R. Cicco, M. M. Talamo, A. Napolitano, V. Augelli, G. M. Farinola, M. D'ischia, *J. Mater. Chem. C* **2013**, *1*, 1018.
- [31] S. Kunimura, T. Ohsaka, N. Oyama, *Macromolecules* **1988**, *21*, 894.
- [32] A. Q. Zhang, C. Q. Cui, Y. Z. Chen, J. Y. Lee, *J. Electroanal. Chem.* **1994**, *373*, 115.
- [33] S. Mu, *Synth. Met.* **2004**, *143*, 259.
- [34] V. Ball, D. D. Frari, V. Toniazio, D. Ruch, *J. Colloid Interface Sci.* **2012**, *386*, 366.
- [35] T. G. Barclay, H. M. Hegab, S. R. Clarke, M. Ginic-Markovic, *Adv. Mater. Interfaces* **2017**, *4*, 1601192.
- [36] L. Zhang, J. Lian, *J. Electroanal. Chem.* **2007**, *611*, 51.
- [37] M. Quinto, A. J. Bard, *J. Electroanal. Chem.* **2001**, *498*, 67.
- [38] N. Nishizawa, A. Kawamura, M. Kohri, Y. Nakamura, S. Fujii, *Polymers* **2016**, *8*, 62.
- [39] A. Ghavaminejad, L. E. Aguilar, R. B. Ambade, S.-H. Lee, C. H. Park, C. S. Kim, *Colloids Interface Sci. Commun.* **2015**, *6*, 5.
- [40] M. B. Clark, J. A. Gardella, T. M. Schultz, D. G. Patil, L. Salvati, *Anal. Chem.* **1990**, *62*, 949.
- [41] J. W. Colson, W. R. Dichtel, *Nat. Chem.* **2013**, *5*, 453.
- [42] M. Bisaglia, S. Mammi, L. Bubacco, *J. Biol. Chem.* **2007**, *282*, 15597.
- [43] Y. Tokura, S. Harvey, X. Xu, C. Chen, S. Morsbach, K. Wunderlich, G. Fytas, Y. Wu, D. Y. W. Ng, T. Weil, *Chem. Commun.* **2018**, *54*, 2808.
- [44] O. Abou Mehrez, F. Dossier-Berne, B. Legube, *Chemosphere* **2016**, *145*, 464.
- [45] A. K. Dhara, K. Kumar, S. Kumari, U. P. Singh, K. Ghosh, *Transition Met. Chem.* **2020**, *45*, 159.
- [46] N. Singh, J. Nayak, K. Patel, S. K. Sahoo, R. Kumar, *Phys. Chem. Chem. Phys.* **2018**, *20*, 25812.
- [47] P. Shi, X. Miao, H. Yao, S. Lin, B. Wei, J. Chen, X. Lin, Y. Tang, *Electrochim. Acta* **2013**, *92*, 341.
- [48] W. Qiang, W. Li, X. Li, X. Chen, D. Xu, *Chem. Sci.* **2014**, *5*, 3018.
- [49] D. Chen, L. Zhao, W. Hu, *J. Colloid Interface Sci.* **2016**, *477*, 123.
- [50] D. Fan, X. Zhu, Q. Zhai, E. Wang, S. Dong, *Anal. Chem.* **2016**, *88*, 9158.
- [51] P. Yang, S. Zhang, X. Chen, X. Liu, Z. Wang, Y. Li, *Mater. Horiz.* **2020**, *7*, 746.
- [52] S. McGraw, E. Alocilja, A. Senecal, K. Senecal, *Biosensors* **2012**, *2*, 465.
- [53] T. Marchesi D'alvise, S. Harvey, L. Hueske, J. Szelwicka, L. Veith, T. P. J. Knowles, D. Kubiczek, C. Flaig, F. Port, K.-E. Gottschalk, F. Rosenau, B. Graczykowski, G. Fytas, F. S. Ruggeri, K. Wunderlich, T. Weil, *Adv. Funct. Mater.* **2020**, *30*, 2000378.
- [54] J. Pollet, F. Delpont, K. P. F. Janssen, K. Jans, G. Maes, H. Pfeiffer, M. Wevers, J. Lammertyn, *Biosens. Bioelectron.* **2009**, *25*, 864.
- [55] I. Antohe (Arghir), K. Schouteden, P. Goos, F. Delpont, D. Spasic, J. Lammertyn, *Sens. Actuators, B* **2016**, *229*, 678.
- [56] A. T. Reiner, N.-G. Ferrer, P. Venugopalan, R. C. Lai, S. K. Lim, J. Dostálek, *Analyst* **2017**, *142*, 3913.
- [57] R. Hasler, C. Reiner-Rozman, S. Fossati, P. Aspermaier, J. Dostálek, S. Lee, M. Ibáñez, J. Binting, W. Knoll, *ACS Sens.* **2022**, *7*, 504.
- [58] S. Hong, J. Kim, Y. S. Na, J. Park, S. Kim, K. Singha, G. Il Im, D. K. Han, W. J. Kim, H. Lee, *Angew. Chem. Int. Ed.* **2013**, *52*, 9187.